A&A, 681, A92 (2024)
https://doi.org/10.1051/0004-6361/202347506

Astronomy & Astrophysics
Special issue

Solar Orbiter First Results (Nominal Mission Phase)

Modelling two energetic storm particle events observed by Solar Orbiter using the combined EUHFORIA and iPATH models

Zheyi Ding[1], Gang Li[2], Glenn Mason[3], Stefaan Poedts[1,4], Athanasios Kouloumvakos[3], George Ho[3], Nicolas Wijsen[5,6], Robert F. Wimmer-Schweingruber[7], and Javier Rodríguez-Pacheco[8]

[1] Centre for mathematical Plasma Astrophysics, KU Leuven, 3001 Leuven, Belgium
[2] Department of Space Science and CSPAR, University of Alabama in Huntsville, Huntsville, AL 35899, USA
e-mail: gangli.uah@gmail.com
[3] Johns Hopkins Applied Physics Lab, Laurel, MD 20723, USA
[4] Institute of Physics, University of Maria Curie-Skłodowska, Pl. M. Curie-Skłodowska 5, 20-031 Lublin, Poland
[5] Heliophysics Science Division, NASA Goddard Space Flight Center, Greenbelt, MD 20771, USA
[6] Department of Astronomy, University of Maryland College Park, College Park, MD 20742, USA
[7] Institute of Experimental and Applied Physics, University of Kiel, Leibnizstrasse 11, 24118 Kiel, Germany
[8] Universidad de Alcalá, Alcalá de Henares 28805, Spain

Received 19 July 2023 / Accepted 10 November 2023

ABSTRACT

Context. By coupling the EUropean Heliospheric FORcasting Information Asset (EUHFORIA) and the improved Particle Acceleration and Transport in the Heliosphere (iPATH) models, we model two energetic storm particle (ESP) events originating from the same active region (AR 13088) and observed by Solar Orbiter (SolO) on August 31, 2022, and September 5, 2022.
Aims. By combining numerical simulations and SolO observations, we aim to better understand particle acceleration and the transport process in the inner heliosphere.
Methods. We simulated two coronal mass ejections (CMEs) in a data-driven, real-time solar wind background with the EUHFORIA code. The MHD parameters concerning the shock and downstream medium were computed from EUHFORIA as inputs for the iPATH model. In the iPATH model, a shell structure was maintained to model the turbulence-enhanced shock sheath. At the shock front, assuming diffuse shock acceleration, the particle distribution was obtained by taking the steady state solution with the instantaneous shock parameters. Upstream of the shock, particles escape, and their transport in the solar wind was described by a focused transport equation using the backward stochastic differential equation method.
Results. While both events originated from the same active region, they exhibited notable differences. One notable difference is the duration of the events, as the August ESP event lasted for 7 h, while the September event persisted for 16 h. Another key difference concerns the time intensity profiles. The September event showed a clear crossover upstream of the shock where the intensity of higher energy protons exceeds those of lower energy protons, leading to positive ("reverse") spectral indices prior to the shock passage. For both events, our simulations replicate the observed duration of the shock sheath, depending on the deceleration history of the CME. Imposing different choices of escaping length scale, which is related to the decay of upstream turbulence, the modelled time intensity profiles prior to the shock arrival also agree with observations. In particular, the crossover of this time profile in the September event is well reproduced. We show that a "reverse" upstream spectrum is the result of the interplay between two length scales. One characterizes the decay of the accelerated particles upstream of the shock, which are controlled by the energy-dependent diffusion coefficient, and the other characterizes the decay of upstream turbulence power, which is related to the process of how streaming protons upstream of the shock excite Alfvén waves.
Conclusions. The behavior of solar energetic particle (SEP) events depends on many variables. Even similar eruptions from the same AR may lead to SEP events that have very different characteristics. Simulations taking into account real-time background solar wind, the dynamics of the CME propagation, and upstream turbulence at the shock front are necessary to thoroughly understand the ESP phase of large SEP events.

Key words. acceleration of particles – shock waves – Sun: corona – Sun: coronal mass ejections (CMEs) – Sun: heliosphere – Sun: particle emission

1. Introduction

In large solar energetic particle (SEP) events, protons and ions can be accelerated to very high energies (>100 MeV/n), causing a severe radiation hazard in space weather (Desai & Giacalone 2016). Solar energetic particle events are typically associated with shock waves driven by coronal mass ejections (CMEs), and the acceleration mechanism is thought to be diffusive shock acceleration (DSA; Axford et al. 1977; Drury 1983). When a steady-state solution is considered, the DSA predicts a power law spectrum for energetic particles. Observations of many SEP events indeed show that power laws can, in general, provide a good description of SEP spectra. However, careful examination of individual events shows that there is a large variability

from event to event. That is, events with similar eruption characteristics can vary significantly in maximum particle energy, particle composition, and spectral shape. Even for the same event, different observers connecting to different parts of the shock may see different SEP characteristics (e.g., Dresing et al. 2014; Mason et al. 2012; Desai et al. 2016; Kouloumvakos et al. 2019).

The recent Solar Orbiter (SolO) and Parker Solar Probe (PSP) missions have gathered unprecedented data of energetic particles near the Sun, including some unexpected measurements of SEP events. These measurements offer new clues to better understand the outstanding problem of charged particle energization and propagation (see review by Malandraki et al. 2023). These observations suggest that there are still many factors that can affect the particle acceleration process and that they require more detailed examination. In situ observations of SEP events involve the interplay of acceleration and transport. At the shock front, energetic particles are continuously accelerated. After being accelerated, they escape upstream and propagate and cross the interplanetary magnetic field (IMF) lines and reach an observer. The observed ion time profiles and ion spectra are therefore controlled both by the acceleration and the transport process. At the shock passage, there is a phase of the SEP event where local shock parameters and local energetic particles (often signaled by a peak around the shock passage) are observed simultaneously. This phase is often referred to as an energetic storm particle (ESP) event (Bryant et al. 1962). It has been argued that the study of these events can single out the acceleration process (e.g., Santa Fe Dueñas et al. 2022; Lario et al. 2018, 2023; Ding et al. 2023). However, due to enhanced turbulence near the shock complex, downstream of the shock, energetic particles accelerated earlier become trapped within the shock complex. This fact makes the interpretation of downstream particle behavior very difficult.

Our understanding of the acceleration process in ESP events is further complicated by the transport process upstream of the shock. The presence of turbulence in the upstream region is essential for the scattering and escape of energetic particles. It is commonly assumed that the turbulence near the shock takes the form of Alfvén waves, and upstream of the shock, these waves are driven by protons streaming away from the shock front. This leads to a coupling between the wave intensity and the anisotropy of the particle distribution function (Bell 1978). An earlier attempt to examine the effect of these waves on the particle acceleration process in the context of interplanetary shocks was taken by Lee (1983), who solved the coupled particle transport and upstream Alfvén wave intensity equations and obtained analytical solutions under the steady-state assumption. Later, Gordon et al. (1999) utilized the steady-state solution for both the energetic particles and upstream wave spectra to examine particle acceleration at Earth's bow shock. For traveling shocks, such as those driven by CMEs, the particle acceleration is intrinsically a time-dependent problem. Ng et al. (2003) adopted the same set of equations as Lee (1983) but solved the time-dependent wave transport equation, enabling the determination of wave action and energetic particle spectra in a time-dependent manner.

Modelling a time-dependent particle acceleration process is itself time-consuming. One approach that has been proven to be successful in modelling large SEP events (Verkhoglyadova et al. 2009, 2010) was developed in the Particle Acceleration and Transport in the Heliosphere (PATH) code (Zank et al. 2000; Rice et al. 2003; Li et al. 2003, 2005b). The PATH model tracked the propagation of the CME-driven shock numerically and evaluated the instantaneous dynamic timescale of the CME-driven shock. At any given time, the solution of the wave intensity, although intrinsically a time-dependent problem, can be approximated by a steady-state solution at the shock front, with the maximum particle energy constrained by the instantaneous shock dynamic timescale, as given by Gordon et al. (1999). Such an approach is further elaborated in the improved PATH (iPATH) model (Hu et al. 2017, 2018) and in the investigation of individual events (Li et al. 2021; Ding et al. 2020, 2022). In this work, we follow the same approach and combine the iPATH code with the EUropean Heliospheric FORcasting Information Asset (EUHFORIA; Pomoell & Poedts 2018) code. In contrast to previous work, we do not attempt detailed event fitting. Instead, we pay special attention to various length scales upstream of the shock and how their relative size can affect the observed features of SEP events. Specifically, by comparing two recent ESP events observed by SolO, we aim to understand the interplay between upstream turbulence and the decay of particle intensity upstream of the shock. We analyze the characteristics of upstream magnetic fluctuation and elucidate the underlying mechanisms of particle escape from the shock. These analyses were achieved by utilizing the combined EUHFORIA and iPATH models to simulate the observed time-intensity profiles and spectra. Our analyses form a basis for understanding different types of ESP phases of SEP events.

Our paper is organized as follows. In Sect. 2, we briefly discuss the coupling between the EUHFORIA and iPATH models, explaining how shock parameters and shell structures are extracted from EUHFORA and passed to iPATH and how particles are accelerated at the shock front and trapped behind the shock front in the shells in the iPATH model. Section 3 contains the analyses for the two events observed by SolO. The observed upstream wave intensities are used to obtain the turbulence decay timescales for both events. These timescales are used to drive the effective length scale of enhanced upstream turbulence in the iPATH model. The observed duration of the enhanced downstream turbulence was compared with the shell width from the simulations. We also carefully discuss the escape process upstream of the shock. For a particular energy-dependent choice of the escape length, qualitative agreements between observation and simulation can be obtained. The main conclusions of this work are summarized in Sect. 4.

2. Model setup

2.1. Modelling a coronal mass ejection and its driven shock

The EUHFORIA model is a comprehensive data-driven coronal and heliospheric model specifically designed for space weather forecasting. It combines two major modules to simulate the realistic solar wind conditions of the inner heliosphere: the empirical coronal model and the heliospheric magnetohydrodynamic (MHD) model (Pomoell & Poedts 2018). In this study, the CME is simulated using the Cone model (Zhao et al. 2002; Odstrcil et al. 2004). The cone model simulates the CME as a hydrodynamic cloud of plasma with increased density and temperature. It is inserted into the solar wind with a constant speed and angular width. We adopted CME parameters in the Space Weather Database Of Notifications, Knowledge, Information[1] (DONKI) and in the CDAW catalog[2] as references. The in situ plasma and magnetic field measurements provide information on the arrival of the shock and the solar wind conditions upstream

[1] https://kauai.ccmc.gsfc.nasa.gov/DONKI/
[2] https://cdaw.gsfc.nasa.gov/CME_list/HALO/halo.html

Table 1. Input parameters of the Cone CME model in EUHFORIA.

Parameter	Event 1	Event 2
Insertion time	2022-08-30T20:29:00	2022-09-05T18:24:00
Insertion latitude (HEEQ)	−15°	−25°
Insertion longitude (HEEQ)	150°	175°
Half-width	50°	40°
Speed	1000 km s^{-1}	2200 km s^{-1}
Density	4.0×10^{-18} kg m^{-3}	0.5×10^{-18} kg m^{-3}
Temperature	2.0×10^6 K	2.0×10^6 K

and downstream of the shock. The kinematic insertion parameters (the CME speed and density) are fine-tuned to match the shock arrival time and in situ plasma measurements at SolO. The specific parameters for the insertion of the Cone CME in two events are provided in Table 1. Grid resolutions in EUHFORIA are as follows: 1024 grid cells in the radial direction between 0.1 au and 2.0 au, and a 4° angular resolution in longitudes and latitudes.

In the context of studying CME-driven shocks in EUHFORIA, it is essential to accurately identify the shock structure. To achieve this, we adopted the methodology described in Ding et al. (2022). The initial step was the identification of shock positions within the simulation. Once the shock locations were determined, we calculated several important shock parameters, including the shock speed, shock compression ratio, and shock obliquity. The shock locations and the shock parameters serve as crucial inputs for the iPATH model, which considers the dynamics variation of CME-driven shocks and flow conditions upstream and downstream of the shock.

2.2. The iPATH model

A detailed discussion of the iPATH model can be found in Hu et al. (2017). In this section, we briefly discuss the structures of the iPATH model and the parameters in the iPATH model that are relevant to our current work. The iPATH model contains three modules: (1) an MHD module that simulates the background solar wind and the CME-driven shock and tracks the downstream shell structures; (2) a particle acceleration module that computes particle spectra at the shock front; and (3) a particle transport module that follows the propagation of particles escaping upstream of the CME-driven shock. In this work, we use EUHFORIA to replace the MHD module of the iPATH code. The coupling of the EUHFORIA and iPATH models was introduced in Ding et al. (2022), which is similar to the approach taken in Li et al. (2021), where the authors coupled the Alfvén Wave Solar Model (AWSoM; van der Holst et al. 2010) with the iPATH to provide a more realistic description of the CME-driven shock.

Following Ding et al. (2020, 2022), Li et al. (2021), we describe the instantaneous particle distribution function at the shock by

$$f(\mathbf{r}, p, t_k) = c_1 \epsilon_{\mathbf{r}} n_{\mathbf{r}} p^{-\beta} H[p - p_{\mathrm{inj},\mathbf{r}}] \exp\left[-\left(\frac{E}{E_{0,\mathbf{r}}}\right)^{\alpha}\right], \quad (1)$$

where $\beta = 3s_{\mathbf{r}}/s_{\mathbf{r}} - 1$, $s_{\mathbf{r}}$ is the shock compression ratio at $\mathbf{r}$(r, θ,ϕ), $\epsilon_{\mathbf{r}}$ is the injection efficiency, $n_{\mathbf{r}}$ is the upstream solar wind density, $p_{\mathrm{inj},\mathbf{r}}$ is the particle injection momentum, and $E_{0,\mathbf{r}}$ is the kinetic energy that corresponds to a maximum proton momentum $p_{\mathrm{max},\mathbf{r}}$. The exponential tail $\exp(-(E/E_0)^{\alpha})$ accounts for the finite shock extension and finite acceleration time, and α is a free parameter that describes the steepness of the exponential tail. Just as in Ding et al. (2022), we adopted $\alpha = 2$. We assumed the injection rate to be 0.5% at the parallel shock. The term H is the Heaviside function, and c_1 is a normalization constant given by

$$c_1 = 1/\int_{p_{\mathrm{inj},\mathbf{r}}}^{+\infty} p^{-\beta} H[p - p_{\mathrm{inj},\mathbf{r}}] * \exp\left[-\left(\frac{E}{E_{0,\mathbf{r}}}\right)^{\alpha}\right] d^3p. \quad (2)$$

In the 2D iPATH model (Hu et al. 2017), the accelerated particles that convect with the shock and the diffuse downstream of the shock are tracked using a shell model. A 3D version of the shell model has been developed with the data-driven MHD models (Li et al. 2021; Ding et al. 2022), where individual shells are divided into multiple parcels that are labelled by their longitudes and latitudes. The angular resolution is 4 degrees, which is the grid resolution of EUHFORIA. Following Ding et al. (2022), we only considered the evolution of the shell along the radial direction. For a given (θ, ϕ), the outer edge of the outermost shell is given by the shock front r_i (i is the number of time steps) at time t_i. Other shells with the same (θ, ϕ) have their outer edges at radial distances r_j ($j = 1, 2, \ldots, i-1$), which are functions of time. At time t_i, r_j is given by

$$r_j(t_i) = r_j(t_{i-1}) + \int_{t_{i-1}}^{t_i} u(r_j(t_{i-1} + t'), \theta, \phi) \mathrm{d}t', \quad (3)$$

where u is the solar wind speed at the shell location (r_j, θ, ϕ) at successive MHD time steps. In discrete form, Eq. (3) becomes

$$r_j(t_i) = r_j(t_{i-1}) + u(r_j(t_{i-1}), \theta, \phi)(t_i - t_{i-1}). \quad (4)$$

Equation (4) enables us to construct all the parcels within the shell using the outputs of the EUHFORIA model. The shell model in iPATH is constructed via the realistic 3D shock fronts and time-dependent downstream flow speed from the underlying MHD code. It therefore captures the spatial extension of the downstream region of the shock. For different events, the shell extension can differ significantly. We note that as an implicit assumption in the iPATH model, the turbulence is assumed to be much enhanced in the shells. This implies that a realistic shell model can be used to understand the duration of the shock sheath, where enhanced turbulence is often found. We also note that the duration of the shock sheath can serve as a good approximation of the duration of the ESP phase. This is because if the CME is composed of closed field lines, then to first approximation, particles accelerated at the shock front, presumably along open field lines, cannot penetrate into the CME ejecta. However, if the ejecta contains a significant amount of open field lines, SEPs can indeed penetrate into CME ejecta. Depending on how many open field lines are present, a decrease in SEP intensity

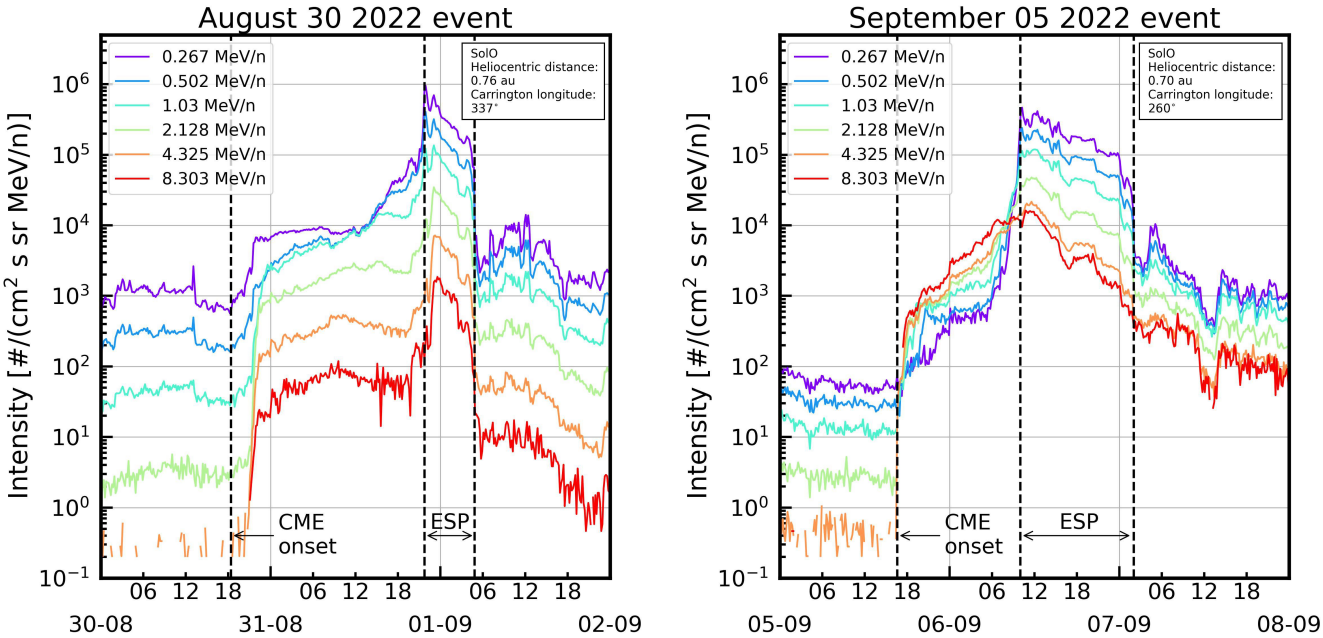

Fig. 1. Proton time intensity profiles for the August 30, 2022 (left) and the September 5, 2022 (right) events as observed by SolO/SIS. The energy range is from 0.267 MeV/n to 8.303 MeV/n. The three dashed lines in each panel indicate the onset time of the CME (left), the arrival time of the IP shock (middle), and the end of the ESP event at SolO (right).

is expected. Because different shells are constructed when the shock is at different times, the resulting energetic particle distributions in these shells are therefore different. As the shock propagates out in time, these different energetic particle populations will be mixed since these particles can diffuse and convect among different parcels (Hu et al. 2017; Ding et al. 2020). This mixing leads to a time-dependent downstream energetic particle distribution, which can be compared to observations.

When particles diffuse far enough upstream of the shock, they can escape. We discuss the process of particles escaping upstream of the shock in Sect. 3.2. In the iPATH model, the transport of these particles in the solar wind is described by a focused transport equation. We follow Ding et al. (2022) in modelling this transport process.

3. Results

3.1. Solar Orbiter observations

We utilized in situ measurements of solar energetic particles, plasma, and magnetic fields obtained by the Suprathermal Ion Spectrograph (SIS) within the Energetic Particle Detector (EPD) suite (Rodríguez-Pacheco et al. 2020; Wimmer-Schweingruber et al. 2021), Solar Wind Analyser (Owen et al. 2020), and MAG magnetometer (Horbury et al. 2020) onboard SolO. These measurements are available most of the time between August 30, 2022, and September 8, 2022, providing an excellent opportunity for comprehensive analysis and comparison of the two ESP events. In this study, our focus is on analyzing the proton intensity measurements obtained by the EPD/SIS instrument and comparing them with the simulated results generated by the combined EUHFORIA and iPATH models. The recent measurements conducted by the EPD/SIS instrument have provided valuable insights into the energetic and suprathermal ion composition in various energetic particle events, including quiet-time ion composition (Mason et al. 2021b, 2023), large and small SEP events (Ho et al. 2022; Bučík et al. 2023; Mason et al. 2021a,b), and corotating interaction region (CIR) events (Allen et al. 2021). Some recent unexpected observations of SEP and SIR-related ion events by the EPD are summarized in the review of Malandraki et al. (2023). The EPD/SIS sensor has demonstrated exceptional sensitivity, enabling precise measurements of the intensity of low-energy channels.

Figure 1 shows the 10-min average proton time intensity profiles observed by SolO/SIS for the August 30 and the September 5 events. The plot shows the average of the SIS sunward and anti-sunward telescopes. Six energy channels ranging from 0.267 to 8.303 MeV/n were selected for analysis. Several notable characteristics emerged when comparing these two events. Firstly, the durations of the ESP events differ significantly, with the August event lasting for approximately 7 h and the September event extending over a period of 16 h. These durations correspond to the passage of the shock-sheath structure associated with each event. The duration of the particles being trapped upstream of the shock is difficult to determine precisely, which is energy-dependent and affected by the transport effects. We note that SolO was located at similar solar distances during the August event (0.76 au) and the September event (0.7 au). Secondly, in the September event, the intensities of the low-energy protons near the shock are lower than that of high-energy protons, resulting in a unique "crossover" feature in the time profiles prior to the arrival of the shock. We note that this crossover is different from the phenomenon related to the velocity dispersion seen near the onset of the SEP events (e.g., Mason et al. 2012; Wu et al. 2023). There, both lower- and higher-energy particles are injected close to the Sun at the same time, and the higher-energy particles arrive at the observer first. The crossover in our event occurs close to the shock, and as we discuss further in this section, it is caused by a long-lasting turbulence-enhancement upstream medium. Such a behavior is rare in gradual SEP events, and to our knowledge, only one similar event has been reported by Lario et al. (2021), who analyzed the November 29, 2020 event observed by the PSP. They suggested that such a time profile could be related to pre-existing interplanetary coronal

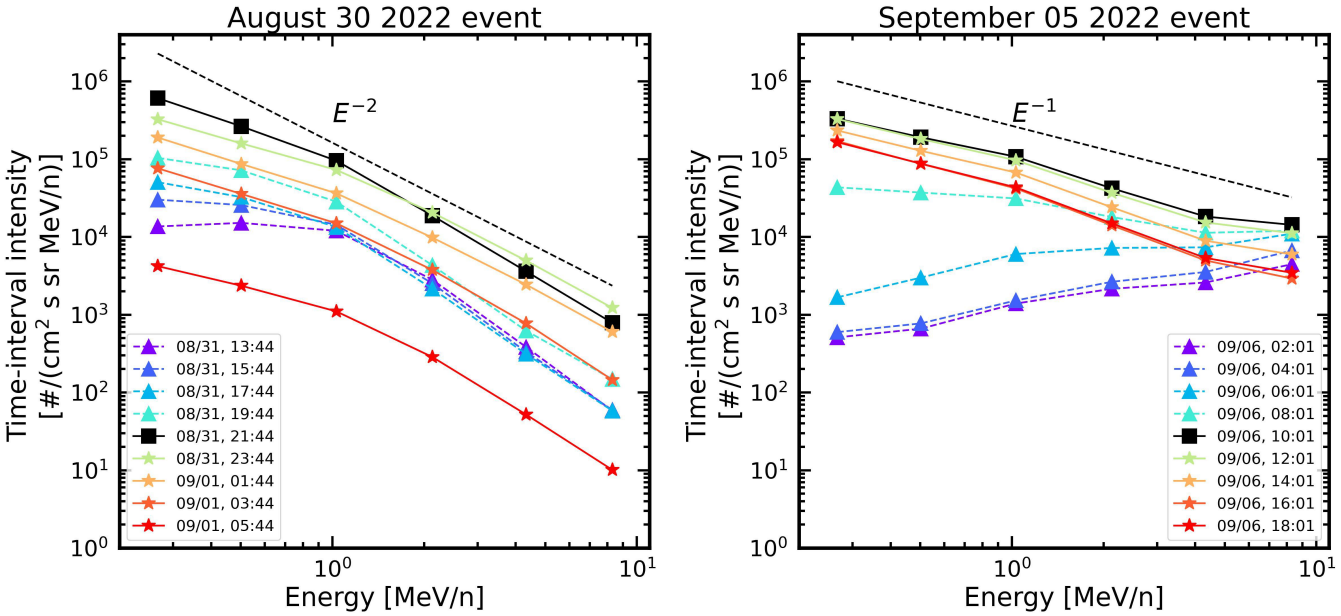

Fig. 2. Two-hour time-interval proton spectra for the August 30, 2022 (left) and the September, 5 2022 (right) events as observed by SolO/SIS from 0.267 MeV/n to 8.303 MeV/n. The times tamps represent the start of the intervals, ranging from 8 h before to 8 h after the arrival of the shock. The black curve with squares corresponds to the time of shock arrival. The triangles and stars represent observations upstream and downstream of the shock. The dashed black line is present to guide the eye. The power law index is E^{-2} for the August event and is E^{-1} for the September event. Upstream of the September 5 event, the crossover is clearly visible.

mass ejection (ICME) structures. As we discuss later, we believe this crossover is a feature of particle escape upstream of a CME-driven shock, and its infrequent appearance is related to the escape length of particles, which is in general a function of particle energy and varies from event to event.

Figure 2 presents 2-h time-interval proton spectra for the August 30, 2022 (left) and the September 5, 2022 event (right) as observed by SolO/SIS in the energy range from 0.267 MeV/n to 8.303 MeV/n. We focused on the spectra within an 8-hour window observed upstream and downstream of the shock. During this period, the August event shows mostly a power law with an index of ~ -2, which is normal for SEP events (Ebert et al. 2016; Desai et al. 2016; Santa Fe Dueñas et al. 2022). Upstream of the shock, there is a slight bend-over feature observed for energies below 1 MeV, which is commonly attributed to a transport modulation effect. Compared to the August event, the September event exhibits a distinctly different behavior where the spectra farther out from the shock are positive, power-law-like, and then the spectra transition to a normal, negative power-law-like across the shock. Additionally, the spectra downstream of the shock are harder compared to the August event, with a power law index of approximately -1. The presence of a positive power law in the spectra of the September event, extending up to energies of 8.3 MeV/n, makes it challenging to explain solely based on the transport effects in the solar wind.

We further examined the plasma and magnetic fields measured by SolO for the two events. Figure 3 shows the measurements for the August event. In addition to the observed data, we also include the simulated solar wind density, solar wind speed, and magnetic field magnitude from the EUHFORIA model. Further details of the EUHFORIA simulations are discussed in Sect. 3.3. As shown in Fig. 3, before the arrival of the shock, both the plasma and magnetic field conditions are relatively undisturbed. After the shock, a distinct sheath structure and a magnetic cloud are observed. The duration of the ESP event is clearly bounded by the sheath structure, lasting approximately 7 h. Furthermore, we find that it is worth noting that the peak intensity of high-energy protons in this event occurs within the sheath region approximately 1 h after the shock passage. Two similar events with proton intensity peaks after the shock passage were reported in Giacalone (2012). This differs from the typical ESP events where the peak intensity is usually observed at the location of the shock (e.g., Lario et al. 2018, 2023). Nonetheless, investigating and simulating this particular feature is beyond the scope of this work.

The measurements of plasma and magnetic fields for the September event are shown in Fig. 4. A comparison with the August event reveals more enhanced fluctuations in the flow velocity and magnetic field upstream of the shock. In particular, the azimuthal (ϕ) and the elevation (θ) angles of magnetic direction vary significantly for about 6 h ahead of the shock. Upstream from the shock, the intensities of low-energy particles (e.g., 1.03 MeV and below) are smaller than those of higher energies (e.g., 4 MeV and 8 MeV). Lario et al. (2021) reported a similar crossover ESP event on November 29, 2020. They suggested that the low-energy particles are excluded by an ICME upstream of the shock. However, in that event, the crossover feature did not recover back to normal time profiles after the ICME passed through the PSP, and it was preserved until the shock arrived at the observer. They also compared several historical ESP events with proceeding ICMEs, but those events did not exhibit the crossover feature. Therefore, it is our opinion that preceding ICMEs are not the cause for the observed crossover feature. Indeed, there was no clear magnetic cloud detected upstream of the shock in the September event. We however note that there are intense magnetic fluctuations upstream of the shock, indicating the presence of strong turbulence ahead of it.

To further understand the upstream magnetic fluctuations, we computed the power spectral density (PSD) of the total magnetic field using Welch's method (Welch 1967). The power spectra for both events were calculated with a 2-hour interval prior to the

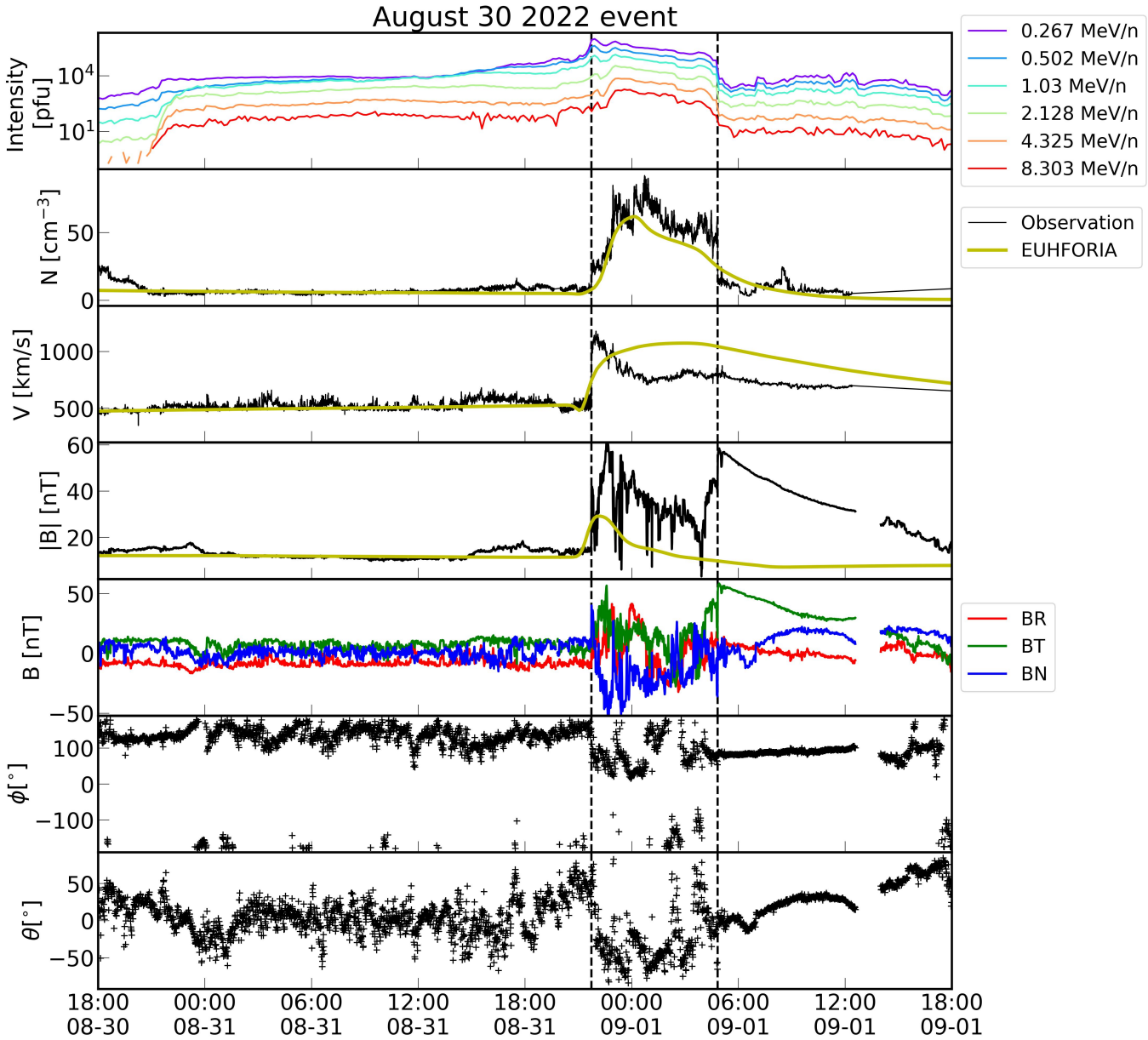

Fig. 3. Solar energetic particle time profiles and in situ plasma and magnetic field for the August 30, 2022 event. The panels present, from top to bottom, the energetic proton time profiles, the solar wind proton number density, the solar wind speed, the magnetic field magnitude, the magnetic field vector measured in the RTN coordinate system, and azimuthal (ϕ) and elevation (θ) angles of the unit vector magnetic field. The yellow lines represent the EUHFORIA simulation results. The dashed lines indicate the IP shock and the end of the ESP event.

shock arrival, as shown in Fig. 5. The left panels of the figure show seven power spectra with a 2-hour interval upstream of the shock. Energetic particles resonate with these waves and the resonance condition is given by the Doppler relation

$$\omega - n\Omega - k_{\parallel}\mu v = 0, \tag{5}$$

where ω is the resonant wave frequency, n is an integer, $\Omega = (Q/A)eB/\gamma m_p c$ is the local ion gyrofrequency, $k_{\parallel}$ is the wave vector component along the background magnetic field, and μ is the particle's pitch angle cosine. In the expression of ion gyrofrequency, v is the particle speed in the plasma frame upstream of the shock; Q and A are the ion charge and mass number, respectively; p is the particle momentum; m_p is the proton mass; γ is the Lorentz factor; and c is the speed of light. Since $\omega = kV_{\rm A}$ for Alfvén waves and $V_{\rm A}$ is much smaller than the particle speed v, then under the extreme resonance broadening condition where $\mu \sim 1$ in Eq. (5), we can obtain the resonance wave number

$$k \approx \frac{Q}{A}\frac{eB}{\gamma\beta_v m_p c^2}, \tag{6}$$

where $\beta_v = v/c$ is the particle speed in units of c. Using Taylor's hypothesis (Taylor 1935), namely, $f = kV_{sw}/2\pi$, the corresponding resonant frequencies that resonate with 0.267, 1.03, and 4.325 MeV protons are marked by vertical lines (from right to left). Away from the shock, the PSD at these frequencies decays significantly (Hu et al. 2013). To clarify the decay rate of the PSD at different frequencies (resonating with different particle energies), the ratio of these PSDs, relative to that closest to the shock (the duration of [−2, 0] h), are plotted versus the corresponding time preceding the shock passage in the middle

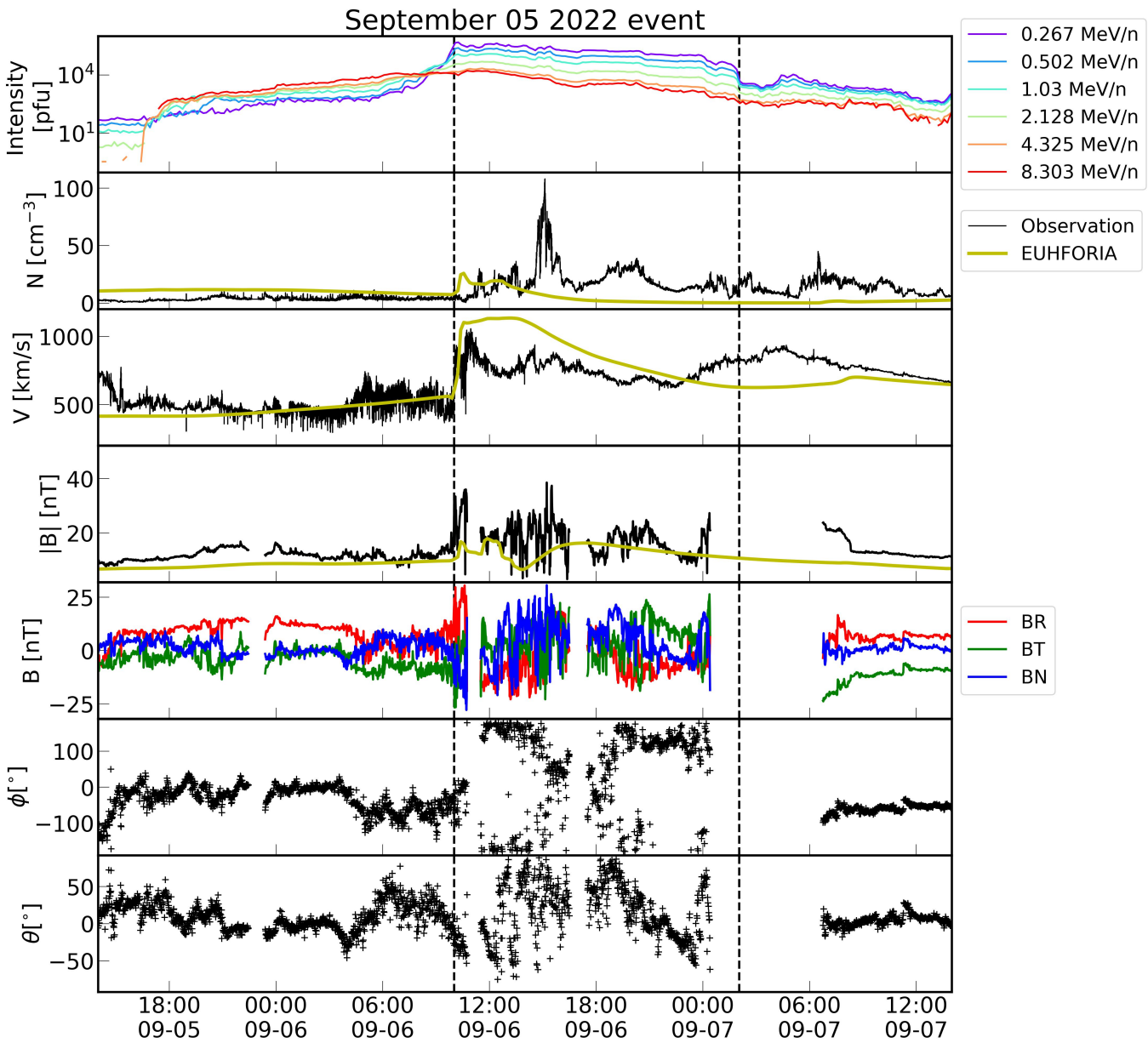

Fig. 4. Same as Fig. 3 but for the September 5, 2022 event.

panels. The decay rates of PSD for these two events differ significantly. For instance, the ratio decreases to 0.1 rapidly after about two hours for the August event, while it takes around six hours to decay to 0.1 for the September event. We then performed a power-law fitting on the spectra between 0.003 Hz to 0.06 Hz. Above 0.06 Hz, the spectra develop a bump-like feature, so we only fit the power spectra between 0.003 Hz to 0.06 Hz. The right panel plots the spectral index as a function of time. We found a significant difference in the spectral slopes between the two events. The September event exhibits a steeper spectral slope of approximately f^{-2} and does not vary for 12 h upstream of the shock, suggesting a well-developed and strong turbulence ahead of the shock (Li et al. 2003).

3.2. Particle escape upstream of the shock

As we demonstrate below, the very different behavior of these two ESP events can be attributed to very different upstream turbulence environments that impact the escape process in these two events. To understand the observations, we examine the escape process in more detail in this section.

We assumed the particle acceleration is due to the first-order Fermi acceleration and the particle scattering is isotropic in the shock frame. At the shock front, the particle distribution function f satisfies the Parker transport equation:

$$\frac{\partial f}{\partial t} + \mathbf{U} \cdot \nabla f = \nabla \cdot (\kappa \nabla f) + \frac{1}{3} \nabla \cdot \mathbf{U} \frac{\partial f}{\partial \ln p} + S - L, \tag{7}$$

where $\mathbf{U}$ is the plasma bulk velocity, κ is the spatial diffusion tensor, and p is the particle momentum. The second term on the left of the equation represents the convection, and the terms on the right represent the spatial diffusion, energy change, sources, and losses, respectively.

Considering a one-dimensional planar shock with an injection momentum p_0, the steady-state solution of f is given by

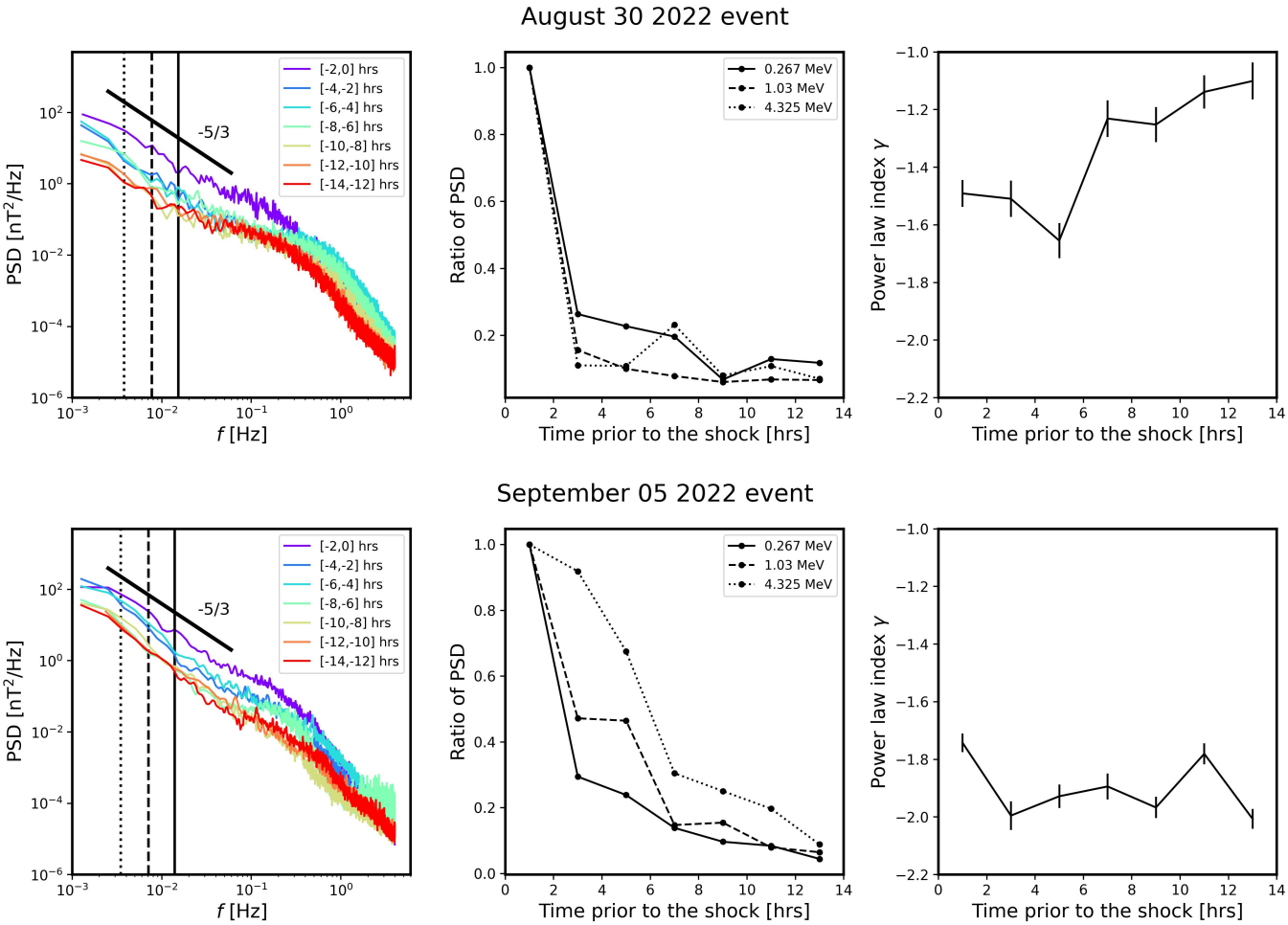

Fig. 5. Total magnetic field Power Spectral Density (PSD) for August 30 2022 (upper) and September 05 2022 (lower) events. The left panels represent the 2-hour interval of PSD as a function of frequency upstream of the shock. The durations are labelled on the top right of the panel. 0 represents the time of shock. The thick solid line shows the power law of $f^{-5/3}$ for reference. The dashed vertical lines indicate the corresponding resonant frequencies of different energies by Taylor's hypothesis. The three energies are labelled in the middle panel. The middle panels show the ratio of PSD as a function of time upstream of the shock, compared to the PSD closest to the shock (i.e., the PSD for the duration of [−2, 0] hours). The right panels show the fitted power law indices in the frequency range [0.003, 0.06] Hz as a function of time.

(e.g., Drury 1983)

$$f(x,p) = Cp^{-3s/(s-1)} H(p-p_0) \exp \int_0^x \frac{U_1}{\kappa_{xx}(x',p)} \mathrm{d}x', \tag{8}$$

where C is a constant; s is the compression ratio; x is the distance to the shock, which is at $x = 0$ ($x < 0$ represents upstream and $x > 0$ represents downstream); U_1 is the upstream speed in the shock frame; $\kappa_{xx}(x,p)$ represents the components of κ along the shock normal direction as a function of x and p; and H is the Heaviside step function. Following Li et al. (2005b), the diffusion coefficient $\kappa_{xx}(x,p)$ is proportional to the wave intensity inverse $I(k_{\rm res},x)^{-1}$ evaluated at the resonant wave number $k_{\rm res}$ as given by Eq. (5), again, assuming the extreme resonance broadening condition. For an x-independent diffusion coefficient $\tilde{\kappa}_{xx}$, which is possible if the wave intensity $I(k,x)$ upstream of the shock is x-independent, the solution of the upstream distribution function has the following form:

$$f(x,p) = Cp^{-3s/(s-1)} H(p-p_0) \exp\left(\frac{-|x|}{L_{\rm diff}(p)}\right). \tag{9}$$

Here, the diffusion length is defined as $L_{\rm diff}(p) = \tilde{\kappa}_{xx}(p)/U_1$. Equation (9) has been examined in many previous studies (e.g., Zank et al. 2000; Li et al. 2003, 2005b; Wijsen et al. 2022), and it signals the exponential decay behavior often seen in SEP observations. Of course, the wave intensity upstream of the shock is not a constant, and it often decays with distance. If we denote $L_{\rm esc}$ as the characteristic length scale describing the decay of upstream wave intensity, then the behavior of the upstream particle distribution depends on the comparison of these two scales. We note that when $I(k,x)$ is x-dependent, one can define $L_{\rm diff}$ using either $I(k,0)$ or some x-averaged $I(k)$.

The exact decay behavior of the wave intensity is unclear and likely event dependent. As a simplified assumption, we considered an exponential increase of the diffusion coefficient upstream of the shock. This leads to an estimation of $\kappa_{xx}(x,p) = \kappa_{xx}(x_0,p)\exp(|x|/L_{\rm esc}(p))$, where $\kappa_{xx}(x_0,p)$ is the diffusion coefficient at the shock (x_0) and $L_{\rm esc}(p)$ is the length scale of the upstream wave intensity. Equation (8) now becomes,

$$f(x,p) = Cp^{-3s/(s-1)} H(p-p_0) \exp\left(-\frac{U_1 L_{\rm esc}(p)}{\kappa_{xx}(x_0,p)}\left(1-\exp\left(-\frac{|x|}{L_{\rm esc}(p)}\right)\right)\right). \tag{10}$$

We note that when the wave intensity decays exponentially away from the shock, the particle intensity upstream of the shock does

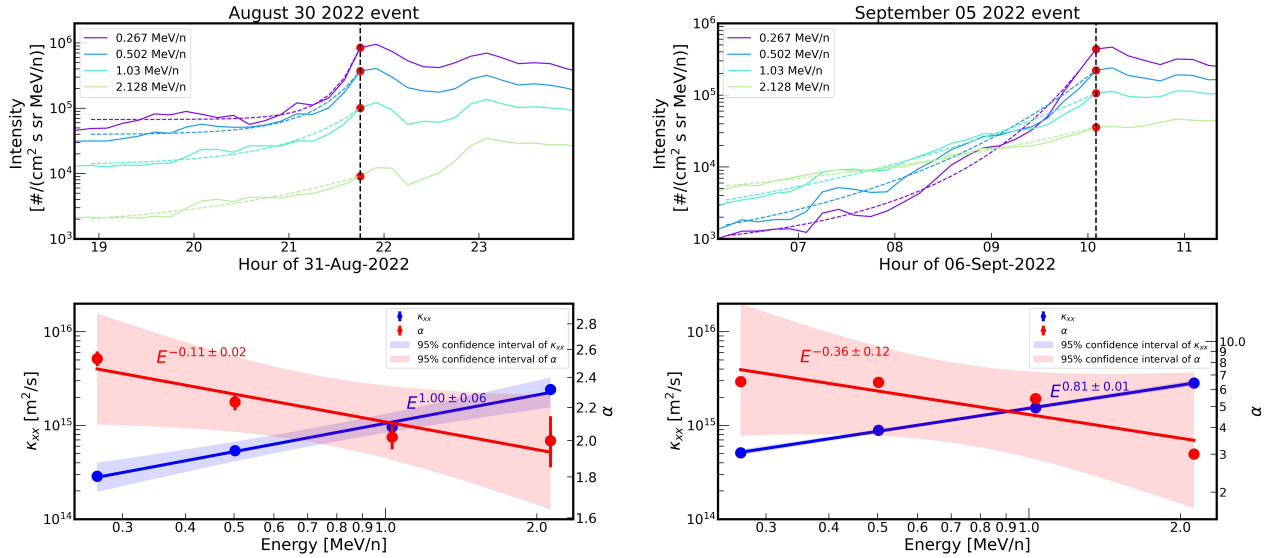

Fig. 6. Upper panels: The solid (dashed) lines represent the observations (fits) of time profiles upstream of the shock by Eq. (10). Lower panel: Diffusion coefficients and the index α as a function of energy for the two events. The lines show the power law fits of the two parameters with 95% confidence interval. See text for details.

not decrease to zero when $|x| \to \infty$, as shown in Eq. (9). Instead, it approaches a constant when $|x| \gg L_{\rm esc}$, indicating that particles can readily escape at some distance from the shock where the turbulence becomes less significant.

The effect of the length scale $L_{\rm esc}$ can be visualized as an escape term f/τ in the transport equation, that is, particles moving to a distance $L_{\rm esc}$ upstream of the shock can escape from the system. This was done in Li et al. (2005a), where the authors introduced the escape term f/τ and related τ to an energy-dependent escape length scale $L_{\rm esc}$. Li et al. (2005a) suggested that the particle distribution function upstream of the shock depends on the ratio of $L_{\rm esc}$ to $L_{\rm diff}$. In previous studies (Zank et al. 2000; Rice et al. 2003; Li et al. 2005b), $L_{\rm esc}$ is typically assumed to be 2–4 times larger than $L_{\rm diff}$. However, this assumption does not hold for the September event, where low-energy particles barely escape from the shock, resulting in the observed crossover profiles. This suggests that $L_{\rm esc}$ should be much larger than $L_{\rm diff}$ and the ratio of $L_{\rm esc}/L_{\rm diff}$ should be energy dependent.

$L_{\rm esc}$ and its momentum dependence can be different for different events. We introduced a parameter α and normalized the escape length to the diffusion length by

$$L_{\rm esc}(p) = \alpha(p) L_{\rm diff}(p). \tag{10}$$

By fitting the upstream time profiles using Eq. (10), we could determine the diffusion coefficient $\kappa_{xx}(x_0, p)$ and $\alpha(p)$ as a function of energy. Figure 6 shows the energy dependence of the diffusion coefficient and the magnitude of α for both events. The distance x is obtained from a measurement in time by assuming a constant shock speed during this period ($x = V_{\rm shock} \cdot {\rm d}t$), where d$t$ is the time from the shock passage. In the figure, we focus on the energies from 0.267 MeV/n to 2.128 MeV/n since the data of 4.325 MeV/n and 8.303 MeV/n channels do not yield satisfactory fitting parameters. We found that both events show a similar energy dependence of the diffusion coefficient, indicating a similar particle diffusion behavior near the shock for both events. The values of κ_{xx} are also consistent with some earlier studies (Tan et al. 1989; Giacalone 2012). However, the parameter α differs very much for the two events and has a very different energy dependence. For the August event, α ranges from 2 to 3 and shows a weak energy dependence $\sim E^{-0.11}$, while for the September event, it ranges from 3 to 7 and shows a stronger energy dependence $\sim E^{-0.36}$. So the length scale of enhanced turbulence is larger in the September event, which is consistent with the analysis of the power spectral density of magnetic fluctuations, as shown in Fig. 5. Furthermore, since $\alpha \sim E^{-0.36}$, from Eq. (10) we observed that the exponential decay rate for lower energy is faster than that for higher energy.

Figure 7 schematically illustrates the accelerated particle distribution at the shock with different length scales for the enhanced wave intensity $I(k, x)$. The steady-state solution of Eq. (7) shows that the particle intensity is constant downstream of the shock and exponentially decaying upstream of the shock. The exponential decay is determined by the diffusion length scale $L_{\rm diff}$. The terms L_{p1} and L_{p2} represent the escape boundaries associated with the length scales of enhanced turbulence $L_{\rm esc}$. Particles within the escape boundary are trapped by the self-excited waves, while particles beyond the escape boundary can escape into the ambient solar wind, as indicated by the dashed curves. As shown in Fig. 6, the parameter α of the escape length scale ($L_{\rm esc} = \alpha L_{\rm diff}$) is very different in terms of value and energy dependence for the two events. In Case I, where the escape length scale is short, the escaped particle intensity exhibits a negative spectral index, as shown in the subpanel. This is the most common case from observations. However, in Case II, when the escape boundary extends to a greater distance, the spectral index of the escaped particle intensity can invert and become positive. Figure 7 schematically explains how a crossover and a positive spectral index can occur in the September events. Roughly speaking, the presence of a larger length scale of enhanced turbulence in the September event hinders the escape of low-energy particles, resulting in the observed crossover and the positive spectral index.

3.3. The duration of the energetic storm particle event

Figure 8 shows snapshots of the radial speed of solar wind from the EUHFORIA simulations for the two events, presented in the Heliocentric Earth Equatorial (HEEQ) coordinate system. The corresponding simulated time series of solar wind parameters

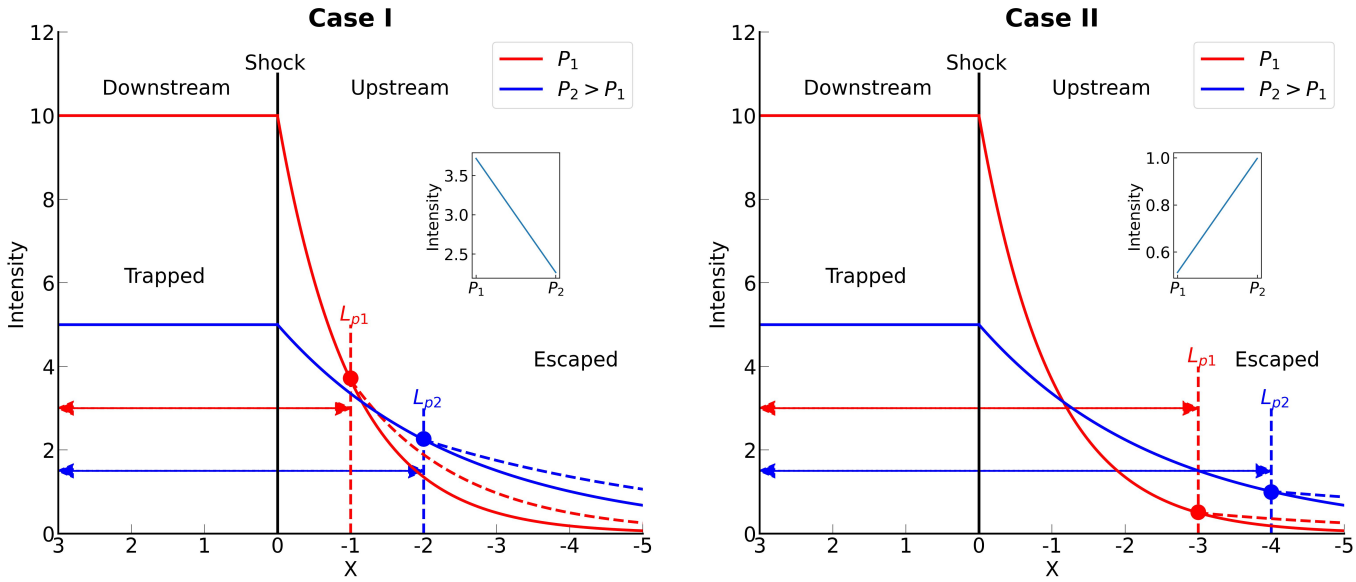

Fig. 7. Two schematics of the distribution of accelerated particles at an interplanetary shock for two momenta P_1 and P_2, adapted from Zank et al. (2006). Both schematics illustrate the momentum-dependent scale length of the exponential decay upstream of the shock and the corresponding trapping and escape of particles. The only difference between the schematics is the different escape length scales L_{p1} and L_{p2}. The subpanel shows the intensity of the escaped particles for P_1 and P_2. The dashed curves ahead of the escape boundary indicate a larger diffusion length scale corresponding to solar wind turbulence. See text for details.

are plotted in Fig. 3 for the August event and in Fig. 4 for the September event. For both events, the simulated magnitudes of the number density and the flow speed near the shock are similar to the observations, providing confidence that EUHFORIA simulations can yield a reasonable description of the shell structures that are to be used in the iPATH model. We note that the cone model does not include the magnetic flux rope and therefore cannot accurately account for the magnetic disturbances. As a result, the simulated magnetic field magnitude is not comparable with SolO measurements. The equatorial and meridional slices of the shell structure are overlaid on top of the CME in Fig. 8. Comparison between these two events provides insights into the different characteristics of the shell structures. Notably, the August event exhibits a smooth shell front, while the September event displays a two-peak shape. This difference arises from the structure of the shock fronts and the evolution of the downstream speed. The two-peak shape of the shock front is a result of the depression caused by a slow stream with high density ahead of the shock nose. Another notable distinction between the events is the radial width of the shell structure. The radial width of the shell structure for the August event is much narrower than that of the September event. This difference is attributed to the different deceleration histories of the plasma speed downstream of the shock. At the inner boundary, the two events have very different CME speeds: 1000 km s^{-1} for the August event and 2200 km s^{-1} for the September event. Observed at SolO, both events have similar downstream speeds of approximately 1000 km s^{-1}. This implies that there is a strong deceleration downstream of the shock for the September event. Consequently, the shell structure is stretched more by the rapid deceleration of the downstream flow. This is particularly evident at the flank of the shock. The deceleration of the shock downstream can also be inferred from the Cone CME parameters. To accurately fit the shock arrival time and the downstream speed observed by SolO, we adopted a small CME density and a small half-width of CME to simulate the pronounced deceleration.

The radial width of the shell structure is essential for understanding the duration of the ESP event. The arrival of the shock front (the first shell) at the observer marks the onset of the ESP event, while the passage of the last shell marks the end of the ESP event. This means that the shell module of the iPATH model can serve as a powerful tool to study ESP events. We remark that a data-driven solar wind model is essential for capturing the downstream dynamics.

To illustrate the history of the shock profile, Fig. 9 shows plots of the time evolution of the shock parameters in the equatorial plane. The three panels from left to right are the shock compression ratio, the shock speed, and the shock obliquity. In each panel, the black curves represent shock fronts at various times from 0.1 au to 1.0 au, with the color scheme indicating the magnitude of the corresponding shock parameters along the shock front. It is assumed that SolO is located in the solar equatorial plane, as its latitude is −3°. Additionally, the white dashed curves represent the Parker field lines passing through SolO at the onset of the event, that is, the left-most vertical dashed lines in Fig. 1. Consider the left panels for the compression ratio. In the August event, SolO was consistently connected to shock regions having a low compression ratio ($s < 3$), even though it is a head-on event. Conversely, in the September event, SolO connects to regions with high compression ratios ($s > 3$). This difference in the compression ratio is in line with the spectral index observed. The August event exhibits a softer spectral index compared to the September event. The middle panel in Fig. 9 depicts the history of the shock speed. The September event shows a speed greater than 2000 km s^{-1} near the inner boundary, whereas the August event has a lower speed of about 1000 km s^{-1}. As discussed earlier, an important feature is the significant deceleration in the September event, as it leads to the larger radial extension of the shell. Finally, the right panels in the figure plot the shock obliquity angle θ_{BN}. In the August event, a smooth transition of shock geometry from quasi-parallel to quasi-perpendicular can be observed as the connection moves from the eastern flank to

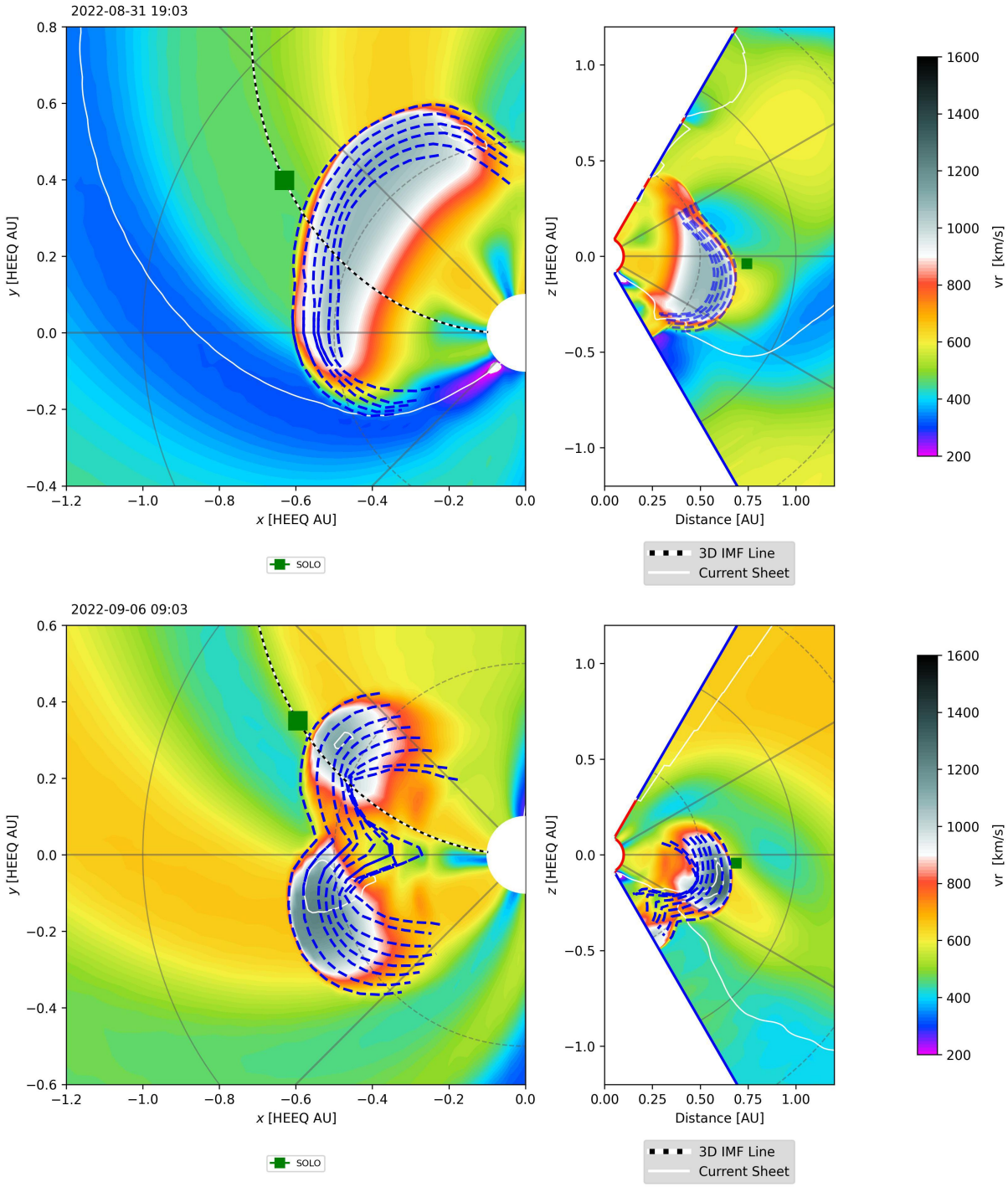

Fig. 8. Equatorial (left) and meridional (right) snapshots of the radial solar wind speed from EUHFORIA for the August 30 (upper) and the September 5 (lower) events. The blue curves show the shell structure behind the shock in the equatorial and meridional planes.

the western flank. The September event shows a large shock obliquity angle in the nose of the shock, resulting from the depression caused by a slow stream ahead of the shock.

3.4. Time profiles and spectra from iPATH model for both events

After calculating the accelerated particle spectra at the shock using Eq. (1), we used Eq. (9) to obtain the escaped particle spectra at a series of times. We tracked the transport of these particles and obtained the corresponding time intensity profiles and spectra at the location of SolO. Figure 10 shows the observed (dashed lines) and modelled (solid lines) 48-h proton time profiles at SolO after the CME eruption. The two critical aspects of this simulation are the accounting for the observed crossover in the time profiles for the September event and the reproduction of the duration of the ESP phases for both events.

With the shell module in the iPATH model we successfully reproduced the durations of the ESP phases for both events. The simulated duration of the ESP phase for the August and

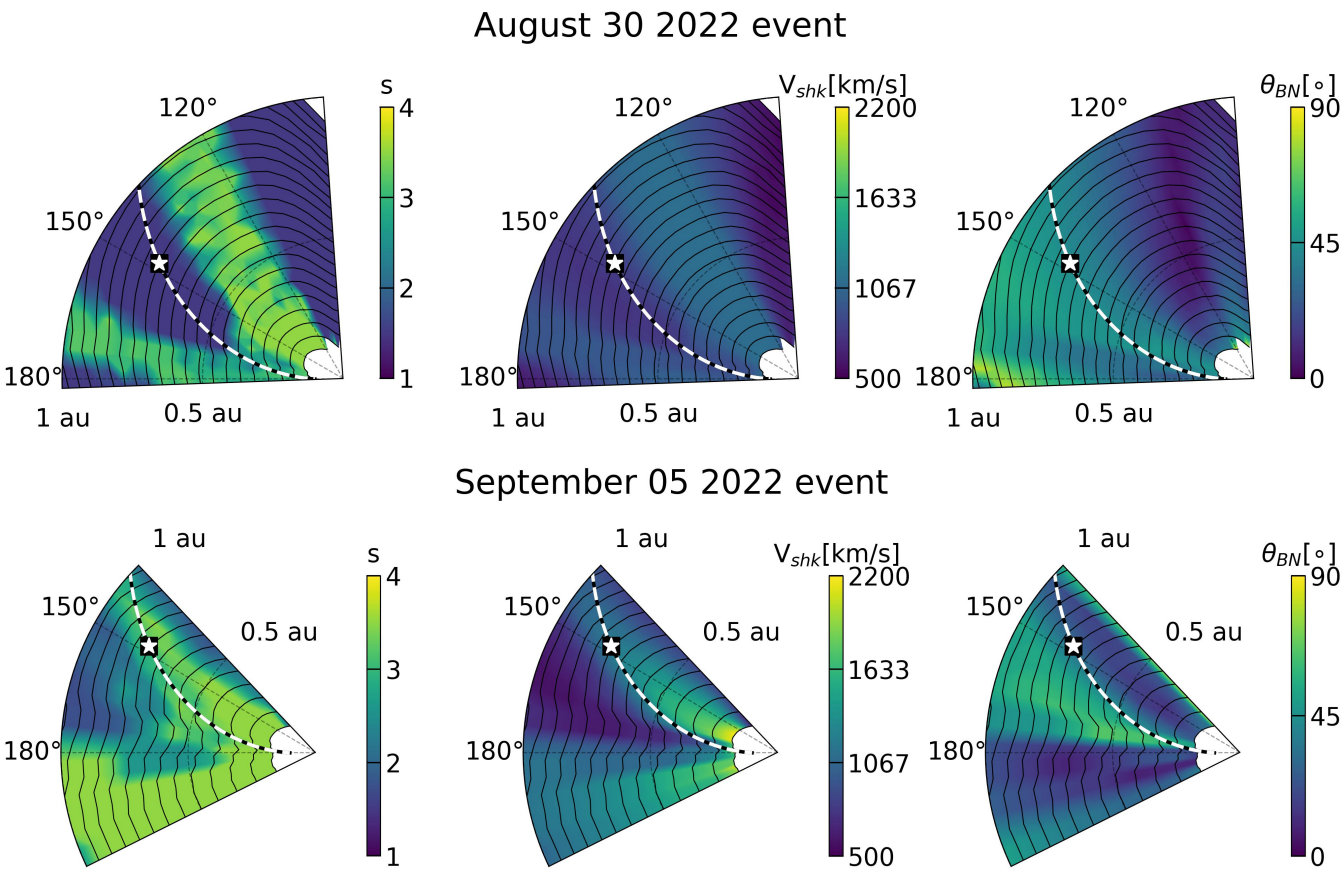

Fig. 9. Evolution of the shock location and shock parameters (compression ratio, shock speed, and obliquity angle) in the equatorial plane from 0.1 au to 1.0 au. The black solid curves show the shock front at different time steps. The color schemes are for different shock parameters along the shock front. The white dashed curves signal the Parker magnetic field lines passing through SolO.

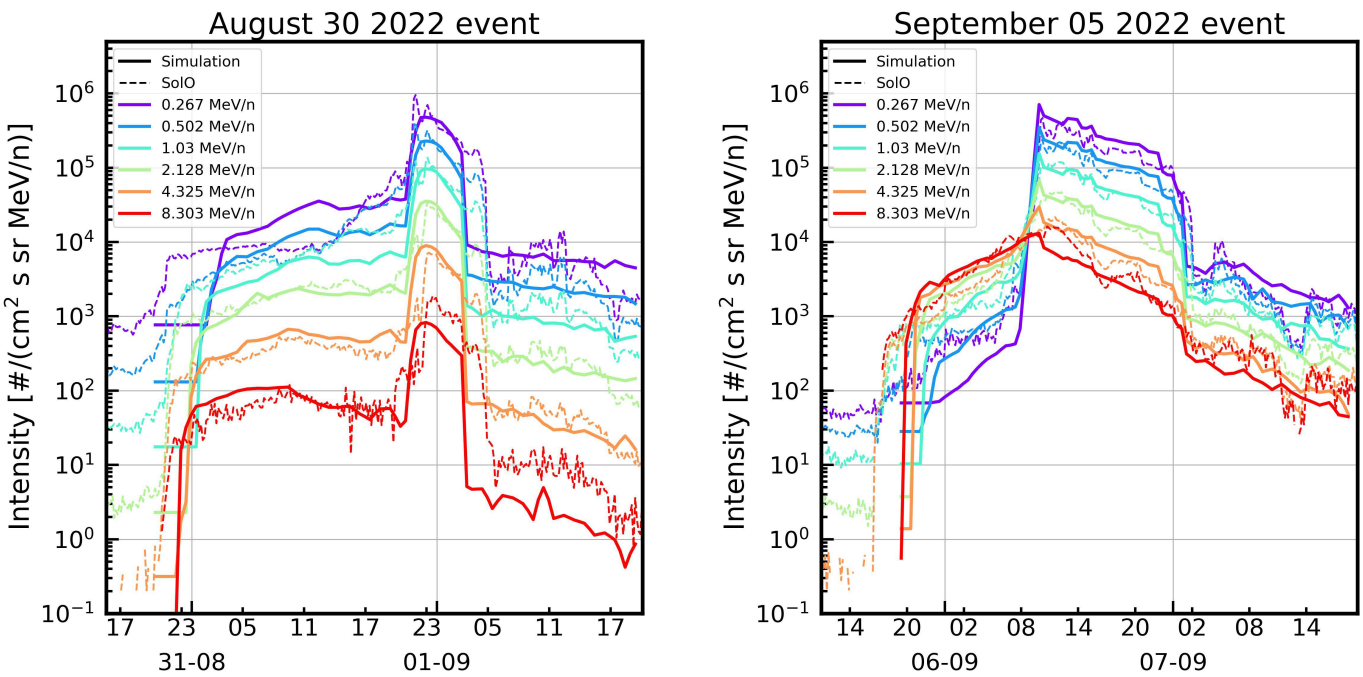

Fig. 10. Time intensity profiles from the SolO observation (dashed lines) and the model calculation (solid lines). The left panel represents the August event, and the right panel represents the September events.

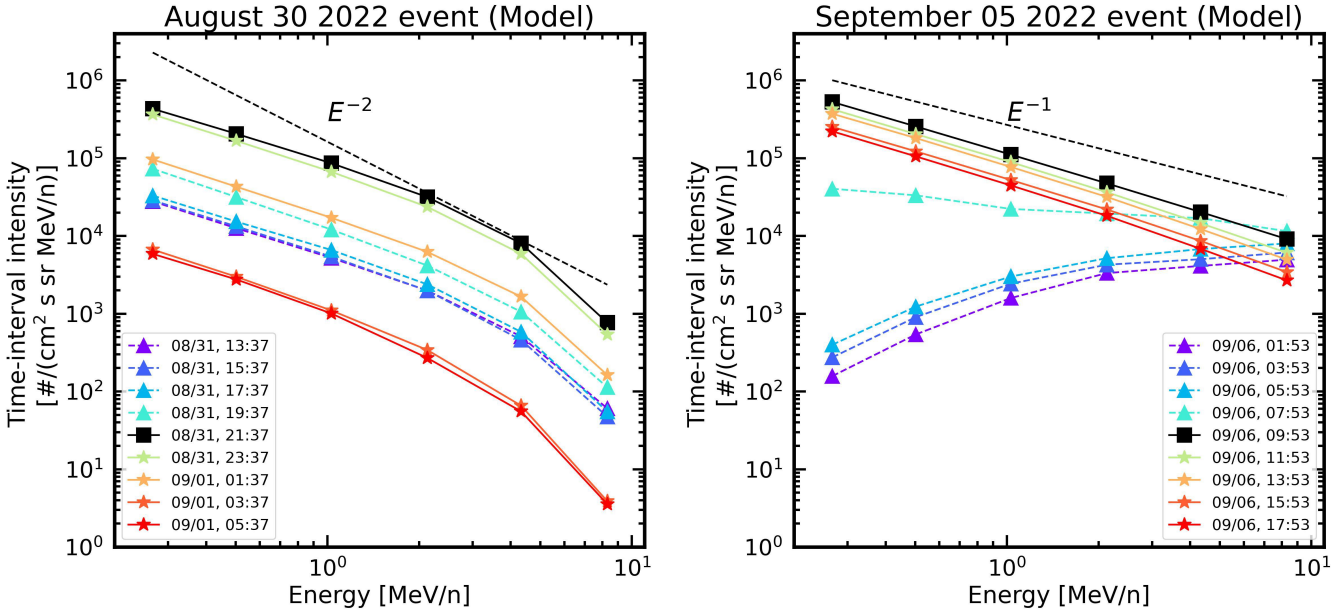

Fig. 11. Two-hour time interval proton spectra from the model calculation (same formats as Fig. 2). The left panel represents the August event, and the right panel represents the September events.

September events are approximately 5 h and 15 h, respectively. This is to be compared with the observations of 7 h and 16 h. The agreement is remarkable, and to our knowledge, this is the first attempt to compare the duration of the ESP phase between simulations and observations, although Li et al. (2003) has already examined the shell structures using a 1D PATH simulation. These results highlight the necessity of using realistic MHD simulations and the shell model in order to better understand ESP events. Additionally, we also modelled the decay of proton intensity in the sheath region attributed to diffusion and convection resulting from the expansion of the shells as described by Zank et al. (2000).

As shown in Fig. 6, the parameter α in the escape length scale ($L_{\rm esc} = \alpha\kappa_{xx}/U_1$) has a very different energy dependence for these two events. We examined how this energy dependence may affect the observed time profile. Using Fig. 6 and observations at 0.7 au as a guide, we assumed

$$\alpha^{\rm Aug}(E) \sim \alpha_0^{\rm Aug}(E/E_0)^0. \quad \alpha^{\rm Sept}(E) \sim \alpha_0^{\rm Sept}(E/E_0)^{-0.4}. \tag{11}$$

For both events, the reference energy is $E_0 = 1.0$ MeV/n. We chose $\alpha_0^{\rm Aug} = 3$ for the August event and $\alpha_0^{\rm Sept} = 5$ for the September event. We note that the energy dependence of α may change as a function of radial distance. However, since we only have in situ observations at $r = 0.7$ au, we do not explore the radial dependence of α in this work.

Our choices of α in Eq. (11) effectively simulate the observed behavior of particle intensity in both events. For the August event, the fitting in Fig. 6 suggests a weak energy dependent of $L_{\rm esc}$, leading to our choice of an energy-independent α in Eq. (11). Particles escape from $L_{\rm esc} = 3L_{\rm diff}$ upstream of the shock. This choice is similar to previous modelling efforts using iPATH (Zank et al. 2000; Li et al. 2003; Hu et al. 2017). The results, as presented in Fig. 10, demonstrate that the modelled time profiles reasonably match the observed data. The intensity exhibits a similar magnitude of decay upstream of the shock, a consequence of the assumption of an energy-independent α. For the September event, the choice of α in Eq. (11) leads to the appearance of the crossover of the time profiles, which qualitatively match the observations. This suggests that the crossover is a consequence of a large α_0 and a stronger energy dependence $(E/E_0)^{-0.4}$. This is an important result of the present work. We note that for the lowest energy channel of 0.267 MeV/n, the modelled intensity is notably lower than the measurements for the September 5 event, suggesting that these particles are trapped and barely escape from the shock in our simulation. This implies that we overestimate the escape length for 0.267 MeV/n protons, and perhaps the energy dependence of α is not a single power law as we assumed. We also find it worth noting that whether crossover can be observed in time profiles is also related to the spectral index of the accelerated particles. It is easier for a crossover to occur for a harder spectrum than for a softer spectrum. This is because the intensity difference between two energies, for example, E_1 and E_2, is larger (smaller) for a softer (harder) spectrum. Therefore, the occurrence of crossover is more likely to occur in events with strong shocks.

We emphasize that the selection of the escape length scale $L_{\rm esc}$ for these two events is based on the in situ observations at $r \sim 0.7$ au, and we assume it has no radial dependence. This suggests that the exact value of $L_{\rm esc}$ is not known a priori and may vary for different events. Further investigations that aim to better understand how $L_{\rm esc}$ vary in different events should be pursued.

Figure 11 shows plots of the simulated particle spectra at intervals of two hours, from eight hours before the shock passage to eight hours after the shock passage. The labels indicate the corresponding start times for each spectrum. To ensure a direct comparison with the observed spectra in Fig. 2, the simulated spectra in Fig. 11 are presented in the same format. In the case of the August event, the modelled spectra exhibit a slightly harder spectrum above 1 MeV/n. compared to the observations. This discrepancy may arise from the fact that the simulated compression ratio is slightly high. For the September event, our model successfully reproduces similar positive spectral indices upstream of the shock and negative indices around −1 downstream of the shock, which are also consistent with the observations. The proper choice of the escape length scale plays a crucial role in understanding this ESP event. If a larger escape length scale is employed, a steeper spectrum with positive spectral indices would be observed. This event serves as an example

highlighting the significance of upstream turbulence in controlling particle acceleration and escape processes.

4. Summary and conclusion

In this study, we investigated two ESP events observed by SolO on August 30, 2022, and September 5, 2022. These two events exhibited different characteristics in terms of ESP duration, time intensity profiles, and spectral slope. The ESP duration of the September event was observed to be significantly longer (∼16 h) compared to the August event (∼7 h). This discrepancy in duration is attributed to the passage of the shock-sheath structure associated with each event. We also compared the proton time intensity profiles and spectra for both events. In the September event, an interesting phenomenon was observed: prior to the arrival of the shock, the flux of low-energy protons was lower than those of high-energy protons, leading to a crossover in time profiles and positive spectral indices. Such behavior is uncommon in ESP events, and only one case was previously reported in Lario et al. (2021). In that event, the authors associated this feature with the presence of a preexisting ICME structure. However, in our case, there was no significant magnetic cloud detected upstream of the shock. Instead, long duration and intense magnetic fluctuations were observed, indicating the presence of strong turbulence ahead of the shock. We calculated the power spectral density of the magnetic fluctuations with a two-hour resolution prior to the shock passage. The PSD analysis revealed very different decay rates of PSD and spectral slopes for the two events. The September event had a long duration (∼6 h) of enhanced turbulence and a steeper spectrum with a spectral index of −2. We found that the longer duration of enhanced turbulence upstream of the shock is crucial for the observed crossover feature of the time profile in the September event.

Properly understanding the crossover requires one to recognize that there are two length scales that control the behavior of the upstream particle distribution function. One length scale is the diffusion scale $L_{\rm diff} = \kappa(x_0, p)/U_1$, with $\kappa(x_0, p)$ as the diffusion coefficient at the shock. It provides an estimate of the decay length scale of particle intensity upstream of the shock. Another scale is the length scale of the upstream turbulence itself, which we denote as $L_{\rm esc}$ in this work. Assuming the turbulence also decays exponentially, which leads to an exponential increase of κ upstream of the shock, the upstream particle distribution function is given by Eq. (10), where the competition of these two length scales is clearly seen through the parameter α, which is the ratio of the escape length scale to the diffusion length ($L_{\rm esc} = \alpha L_{\rm diff}$). The values of α for these two events differ significantly. Furthermore, they also have very different energy dependencies. This difference in α leads to the phenomenon of the crossover and an upstream particle spectrum with a positive spectral index.

We also utilized the combined EUHFORIA and iPATH models to simulate these two events. EUHFORIA provided a good fit of the solar wind density and speed to the in situ measurement, indicating that it captures the dynamic variation of CME deceleration. When EUHFORIA output was fed into the shell module of the iPATH code, we were able to obtain reasonable fits to the duration of ESP events. This is a consequence of the underlying relationship between the radial width of the individual shell and the deceleration of the CME. In the September event, a strong deceleration of the CME leads to a larger radial width of the shell and thus the duration of the ESP events. Furthermore, by choosing a large energy-dependent escape length scale based on the SolO observation, we successfully reproduced the crossover time profiles and the positive spectral indices observed in the September event. These findings highlight the importance of the interplay between the two length scales $L_{\rm diff}$ and $L_{\rm esc}$, one of which characterizes the decay of accelerated particles upstream of the shock, while the other characterizes the duration of the enhanced upstream turbulence power associated with the excitation of Alfvén waves by streaming protons upstream of the shock.

Our main findings are summarized as follows:

1. The combined EUHFORIA-iPATH model, employing a realistic description of the solar wind, provides a reasonable estimate of the duration of the ESP phase for both events. This duration is a consequence of the deceleration history of the CME and the shock it drives, and it requires no free parameters in the model.
2. The observed crossover feature in the time profiles upstream of the shock in the September event highlights the importance of the duration of enhanced upstream turbulence in regulating the behavior of particle distribution function upstream of the shock. A longer duration of enhanced turbulence upstream of the shock, as in the September event, effectively hinders the escape of lower-energy particles from the shock, leading to the crossover phenomena. A criterion for having crossover is encapsulated in the parameter α defined in Eq. (10). Crossover inevitably leads to positive spectral indices of the particle distribution functions upstream of the shock.

It is worth pointing out that other mechanisms beyond DSA may also be responsible for accelerating particles in SEP events. In this study, we only considered the role of DSA; however, several recent studies have shown that particles can be accelerated up to several MeV/n via stochastic magnetic reconnection in dynamical small-scale magnetic islands downstream of shocks and/or inside magnetic cavities (Zank et al. 2015; Khabarova et al. 2015, 2016; Khabarova & Zank 2017; Malandraki et al. 2019). Particles energized via DSA can be trapped by the magnetic islands in the shock sheath. As a result, these energetic particles can be reaccelerated to higher energies and consequently contribute to variations of time intensity profiles during the ESP phase (Khabarova et al. 2021). A detailed examination of particle acceleration at ESP events (particularly of those downstream of the shock) that include such processes should be pursued in future work.

In summary, our findings emphasize that the behavior of upstream turbulence can largely affect particle escape in SEP events. To gain a comprehensive understanding of large SEP events, SEP simulations considering realistic solar wind, CME, and ambient turbulence are crucial. In the future, we will conduct a statistical study examining the effect of the duration of enhanced turbulence upstream of the CME-driven shocks through the parameter α.

Acknowledgements. SolO in-situ data are publicly available at NASA's Coordinated Data Analysis Web (CDAWeb) database (https://cdaweb.gsfc.nasa.gov/index.html/). This work is supported in part by NASA grants 80NSSC19K0075, 80NSSC22K0268, 80NSSC21K1327, and NSF ANSWERS 2149771 at UAH-USA. G.L. also acknowledges support through ISSI team 469. Solar Orbiter is a mission of international cooperation between ESA and NASA, operated by ESA. The Suprathermal Ion Spectrograph (SIS) is a European facility instrument funded by ESA under contract number SOL.ASTR.CON.00004. We thank ESA and NASA for their support of the Solar Orbiter instruments whose data were used in this paper. Solar Orbiter post-launch work at JHU/APL is supported by NASA contract NNN06AA01C and at CAU by German Space Agency (DLR) grant # 50OT2002. The UAH-Spain team acknowledges the financial support by the Spanish Ministerio de Ciencia, Innovación y Universidades FEDER/MCIU/AEI Projects ESP2017-88436-R and PID2019-10

4863RB-I00/AEI/10.13039/501100011033. S.P. acknowledges support from the projects C14/19/089 (C1 project Internal Funds KU Leuven), G.0B58.23N and G.0025.23N (WEAVE; FWO-Vlaanderen), 4000134474 (SIDC Data Exploitation, ESA Prodex-12), and Belspo project B2/191/P1/SWiM. For the computations we used the infrastructure of the VSC-Flemish Supercomputer Center, funded by the Hercules foundation and the Flemish Government-department EWI.

References

Allen, R. C., Mason, G. M., Ho, G. C., et al. 2021, A&A, 656, L2
Axford, W., Leer, E., & Skadron, G. 1977, Int. Cosmic Ray Conf., 11, 132
Bell, A. R. 1978, MNRAS, 182, 147
Bryant, D. A., Cline, T. L., Desai, U. D., & McDonald, F. B. 1962, J. Geophys. Res. Space Phys., 67, 4983
Bučík, R., Mason, G. M., Nitta, N. V., et al. 2023, A&A, 673, L5 (SO Nominal Mission Phase SI)
Desai, M., & Giacalone, J. 2016, Liv. Rev. Sol. Phys., 13, 3
Desai, M. I., Mason, G. M., Dayeh, M. A., et al. 2016, ApJ, 828, 106
Ding, Z.-Y., Li, G., Hu, J.-X., & Fu, S. 2020, Res. Astron. Astrophys., 20, 145
Ding, Z., Wijsen, N., Li, G., & Poedts, S. 2022, A&A, 668, A71
Ding, Z., Li, G., Santa Fe Dueñas, A., et al. 2023, J. Geophys. Res. Space Phys., 128, e2023JA031502
Dresing, N., Gómez-Herrero, R., Heber, B., et al. 2014, A&A, 567, A27
Drury, L. O. 1983, Rep. Prog. Phys., 46, 973
Ebert, R. W., Dayeh, M. A., Desai, M. I., et al. 2016, ApJ, 831, 153
Giacalone, J. 2012, ApJ, 761, 28
Gordon, B. E., Lee, M. A., Möbius, E., & Trattner, K. J. 1999, J. Geophys. Res. Space Phys., 104, 28263
Ho, G. C., Mason, G. M., Allen, R. C., et al. 2022, Front. Astron. Space Sci., 9, 939799
Horbury, T. S., O'Brien, H., Carrasco Blazquez, I., et al. 2020, A&A, 642, A9
Hu, Q., Zank, G. P., Li, G., Ao, X., et al. 2013, AIP Conf. Ser., 1539, 175
Hu, J., Li, G., Ao, X., Zank, G. P., & Verkhoglyadova, O. 2017, J. Geophys. Res. Space Phys., 122, 10,938
Hu, J., Li, G., Fu, S., Zank, G., & Ao, X. 2018, ApJ, 854, L19
Khabarova, O. V., & Zank, G. P. 2017, ApJ, 843, 4
Khabarova, O., Zank, G. P., Li, G., et al. 2015, ApJ, 808, 181
Khabarova, O. V., Zank, G. P., Li, G., et al. 2016, ApJ, 827, 122
Khabarova, O., Malandraki, O., Malova, H., et al. 2021, Space. Sci. Rev., 217, 38
Kouloumvakos, A., Rouillard, A. P., Wu, Y., et al. 2019, ApJ, 876, 80
Lario, D., Berger, L., Wilson, L. B. I., et al. 2018, J. Phys. Conf. Ser., 1100, 012014
Lario, D., Richardson, I., Palmerio, E., et al. 2021, ApJ, 920, 123
Lario, D., Richardson, I. G., Aran, A., & Wijsen, N. 2023, ApJ, 950, 89
Lee, M. A. 1983, J. Geophys. Res. Space Phys., 88, 6109
Li, G., Zank, G. P., & Rice, W. K. M. 2003, J. Geophys. Res. Space Phys., 108, 1082
Li, G., Hu, Q., & Zank, G. P. 2005a, Am. Inst. Phys. Conf. Ser., 781, 233
Li, G., Zank, G. P., & Rice, W. K. M. 2005b, J. Geophys. Res. Space Phys., 110, A06104
Li, G., Jin, M., Ding, Z., et al. 2021, ApJ, 919, 146
Malandraki, O., Khabarova, O., Bruno, R., et al. 2019, ApJ, 881, 116
Malandraki, O. E., Cohen, C. M. S., Giacalone, J., et al. 2023, Phys. Plasmas, 30, 050501
Mason, G. M., Li, G., Cohen, C. M. S., et al. 2012, ApJ, 761, 104
Mason, G. M., Cohen, C. M. S., Ho, G. C., et al. 2021a, A&A, 656, L12
Mason, G. M., Ho, G. C., Allen, R. C., et al. 2021b, A&A, 656, L1
Mason, G. M., Ho, G. C., Allen, R. C., et al. 2023, A&A, 673, L12 (SO Nominal Mission Phase SI)
Ng, C. K., Reames, D. V., & Tylka, A. J. 2003, ApJ, 591, 461
Odstrcil, D., Riley, P., & Zhao, X. 2004, J. Geophys. Res., 109, A02116
Owen, C. J., Bruno, R., Livi, S., et al. 2020, A&A, 642, A16
Pomoell, J., & Poedts, S. 2018, J. Space Weather Space Clim., 8, A35
Rice, W. K. M., Zank, G. P., & Li, G. 2003, J. Geophys. Res. Space Phys., 108, 1369
Rodríguez-Pacheco, J., Wimmer-Schweingruber, R. F., Mason, G. M., et al. 2020, A&A, 642, A7
Santa Fe Dueñas, A., Ebert, R., Dayeh, M., et al. 2022, ApJ, 935, 32
Tan, L. C., Mason, G. M., Gloeckler, G., & Ipavich, F. M. 1989, J. Geophys. Res., 94, 6552
Taylor, G. I. 1935, Proc. R. Soc. London Ser. A-Math. Phys. Sci., 151, 421
van der Holst, B., Manchester, W. B. I., Frazin, R. A., et al. 2010, ApJ, 725, 1373
Verkhoglyadova, O. P., Li, G., Zank, G. P., Hu, Q., & Mewaldt, R. A. 2009, ApJ, 693, 894
Verkhoglyadova, O. P., Li, G., Zank, G. P., et al. 2010, J. Geophys. Res. Space Phys., 115, A12103
Welch, P. 1967, IEEE Trans. Audio Electroacoust., 15, 70
Wijsen, N., Aran, A., Scolini, C., et al. 2022, A&A, 659, A187
Wimmer-Schweingruber, R. F., Janitzek, N. P., Pacheco, D., et al. 2021, A&A, 656, A22
Wu, X., Li, G., Zhao, L., et al. 2023, J. Geophys. Res. Space Phys., e2022JA030939
Zank, G. P., Rice, W. K. M., & Wu, C. C. 2000, J. Geophys. Res. Space Phys., 105, 25079
Zank, G. P., Li, G., Florinski, V., et al. 2006, J. Geophys. Res. Space Phys., 111, 1
Zank, G. P., Hunana, P., Mostafavi, P., et al. 2015, ApJ, 814, 137
Zhao, X., Plunkett, S., & Liu, W. 2002, J. Geophys. Res., 107, 1223